

A WARM MOLECULAR HYDROGEN TAIL DUE TO RAM PRESSURE STRIPPING OF A CLUSTER GALAXY

SURESH SIVANANDAM, MARCIA J. RIEKE, AND GEORGE H. RIEKE¹

Submitted to The Astrophysical Journal

ABSTRACT

We have discovered a remarkable warm (140 – 160 K) molecular hydrogen tail with a mass of approximately $2.5 \times 10^7 M_{\odot}$ extending 20 kpc from a cluster spiral galaxy, ESO 137-001, in Abell 3627. Some portion of this gas is lost permanently to the intracluster medium, as the tail extends beyond the tidal radius of the galaxy. We also detect a hot (580 – 680 K) component in the tail that is approximately 1% of the mass of the warm component. This discovery is direct evidence that the galaxy is currently undergoing ram-pressure stripping, as also indicated by its X-ray and H α tail found by other studies. We estimate the galaxy is losing its interstellar gas at a rate of at least $\sim 1 - 2 M_{\odot} \text{ yr}^{-1}$. If the galaxy persists to lose mass at this estimated rate, it will exhaust its gas reservoir in a single pass through the cluster core, which will take approximately 0.5 – 1 Gyr. The results produced from the modeling of the ram-pressure stripping timescale are consistent with our upper limit and suggest that the effects of ram-pressure are most likely to be seen when the galaxy approaches the outskirts of the cluster core for the first time. We also study the star forming properties of the galaxy and its tail, and we identify most of the previously discovered external H α sources within the tail in our $8\mu\text{m}$ data but not in our $3.6\mu\text{m}$ data, confirming these sources are HII regions. IRS spectroscopy of the region containing these H α sources also reveals aromatic features associated with star formation. We conclude that star-formation is not occurring throughout the molecular hydrogen tail but only immediately downstream of the galaxy. Gas-stripping may be a turbulent process where stars form within high density eddies in the stripped gas.

Subject headings: infrared: galaxies — galaxies: individual (ESO 137-001) — galaxies: clusters: individual (Abell 3627) — galaxies: evolution — galaxies: ISM

1. INTRODUCTION

The morphologies, gas content, and star-forming characteristics of galaxies vary drastically from the cluster to the field environment (see Boselli & Gavazzi (2006) and the references therein). One possible explanation is that gas-rich field galaxies are transformed as they fall into a cluster, during which process they are stripped of their gas and their star formation is halted. However, a complete picture of the transformation of galaxies as they enter the cluster environment is still missing. A variety of processes, such as ram-pressure stripping (Gunn & Gott 1972) and tidal interactions between galaxies (Moore et al. 1996) and the cluster potential (Henriksen & Byrd 1996), are at play. Cortese et al. (2007) suggest that the relative importance of ram-pressure stripping and tidal interactions depends on the mass of the galaxy in question, though their conclusions are hampered by their small sample of two galaxies. Other theoretical studies offer contradictory scenarios for the observed gas deficiency and reduced star formation of cluster spirals. One such study states the transformation starts in group environments (Kawata & Mulchaey 2008) whereas another claims gas loss occurs from gas-only stripping (ram-pressure) events in the cluster environment itself (Tonnesen et al. 2007). Part of the ambiguity arises from the nature of the evidence supporting the existence of ram pressure stripping. Truncated H α disks and HI tails with undisturbed stellar disks

provide circumstantial evidence for a galaxy experiencing ram-pressure stripping (Koopmann & Kenney 2004; Chung et al. 2007). However, it is difficult to address the physical nature of this process from observing such systems due to the absence of direct evidence for interaction with the intracluster medium (ICM).

Spitzer, however, can offer a unique view in observing the interaction between the ICM and galactic interstellar medium (ISM) directly. Appleton et al. (2006) serendipitously discovered powerful molecular hydrogen emission emanating from the intragroup medium (IGM) of Stefan's Quintet. This emission is remarkable because there is hardly any other line emission or even a strong IR continuum. The emission is thought to arise from a high velocity ($\sim 1000 \text{ km s}^{-1}$) collision between an intruding galaxy and a tidal arm (Guillard et al. 2009). Furthermore, through *Spitzer* Infrared Spectrograph (IRS) observations, Appleton et al. (2006) place constraints on the temperature components of the excited gas and its column density by measuring the ground state H₂ vibrational transitions S(0) thru S(5). They make a strong case that the observed lines are shock-excited because the spectrum is dominated purely by molecular hydrogen lines. In addition, there are no aromatic features, which are generally associated with star formation, another source of H₂ emission. The molecular hydrogen line ratios and a total line luminosity that is a large fraction of the total IR emission further corroborate their hypothesis. They show that there are at least two temperature components in the molecular gas: a warm and dense component ($\sim 200\text{K}$) and a hot and sparse component ($\sim 700\text{K}$). Other studies also observe molecular

¹ Steward Observatory, University of Arizona, 933 North Cherry Ave, Tucson, AZ 85721; suresh@as.arizona.edu, mrieke@as.arizona.edu, griek@as.arizona.edu.

hydrogen emission related to shocks and find similar temperature components and little evidence for star formation (e.g. Ogle et al. (2007)). Observing these molecular hydrogen lines (if they exist) around galaxies falling into clusters would be a *direct* probe of gas-stripping processes and would provide quantitative estimates of the amount of gas being stripped.

An excellent candidate for this test is ESO 137-001, a $0.2L_*$ SBC galaxy in the Norma cluster (Abell 3627). ESO 137-001 is a unique galaxy with coaligned X-ray and H α tails that extend approximately 70 and 40 kpc, respectively (Sun et al. 2006, 2007). Its projected distance from the center of the Norma cluster is only 0.28 Mpc. Its low radial velocity (77 km s^{-1}) with respect to the cluster as a whole means most of its motion is in the plane of the sky. Moreover, deep H α imaging reveals bright extraplanar knots along the H α tail that are most likely very large star-forming regions (Sun et al. 2007), suggesting the stripped gas may be forming stars. Deep R $_C$ -band imaging also shows low surface brightness streams that are aligned with the X-ray tail but have a larger width (Woudt et al. 2008). All evidence suggests this galaxy is currently undergoing ram-pressure stripping, making it an ideal candidate for detecting shocked molecular hydrogen.

In this paper we report our discovery of a warm molecular hydrogen tail that trails ESO 137-001. We also discuss the detailed observations of this galaxy with *Spitzer* that support the attribution of its tail to ram pressure stripping and permit the estimation of the resulting mass flow. The paper is structured as follows. In §2, we discuss the details of our observations and data analysis. In §3, we present the results of our analyses. In §4 we discuss the implications of our results. Finally in §5, we list our conclusions. For computing distances, we adopt the concordance cosmological model ($\Omega_\Lambda = 0.73$, $\Omega_m = 0.27$, and $H_0 = 71 \text{ km s}^{-1} \text{ Mpc}^{-1}$). We adopt redshifts provided by the NASA Extragalactic Database of 0.0157 and 0.01544 for the cluster and galaxy, respectively. This yields a luminosity distance of 67.1 Mpc to the cluster and an angular scale of $1'' = 0.316 \text{ kpc}$. All reported errors in this work are quoted at the 1σ level.

2. OBSERVATIONS AND DATA REDUCTION

In this paper we detect and characterize warm molecular H $_2$ emission and resolve the morphology of the stripped gas, and study the star-forming properties of the galaxy and the extraplanar HII regions. To this end, we carried out IRAC imaging and IRS spectral mapping observations. Our IRAC imaging allows us to resolve star-forming regions and study the stellar properties of the galaxy. IRS spectral maps provide detailed information (at a coarser spatial resolution) about the physical properties of the gas such as the strength of the aromatic features, molecular hydrogen lines, and fine-structure lines. The data were taken as part of the *Spitzer* GTO program 50213 (PI: G. Rieke). Three sets of data were taken for the galaxy: The first set of IRS observations done on May 2, 2008 obtained full short-low (SL) and long-low (LL) coverage of the galaxy and LL coverage of its tail. The IRAC data, taken on May 10, 2008, were centered on the galaxy and included all four bands. Finally, the third set of data consisted of follow-up IRS observations done on April 6, 2009, which obtained SL coverage of a

portion of the tail.

2.1. IRAC Imaging

We observed ESO 137-001 in all four (3.6, 4.5, 5.7, and $8\mu\text{m}$) IRAC channels (Fazio et al. 2004). Frame times were kept short to prevent the saturation of the array from Milky Way foreground stars because the galaxy is located at a low galactic latitude ($b \sim -7^\circ$). We obtained a total on source integration time of 260 s in each of the four IRAC channels. We constructed IRAC mosaics of the galaxy with MOPEX (version 18.1.5) using the Basic Calibrated Data (BCD) from the Spitzer pipeline (version S17.2) as input and following the Spitzer Science Center (SSC) IRAC reduction cookbook. Bad pixel rejection was achieved through dithering and median filtering.

2.2. IRS Spectral Mapping

The observations of ESO 137-001 used both the SL and LL IRS modules that together span 5.3 to $38.0 \mu\text{m}$ (Houck et al. 2004). The full wavelength range allows us to observe several ground vibrational state H $_2$ rotational lines, specifically the $\nu=0-0$ S(0) thru S(7) transitions. For the first dataset (May, 2008), we used the IRS BCD from the Spitzer pipeline (version S17.2) along with *CUBISM* (version 1.5) spectral map cube construction software (Smith et al. 2007) to generate spectral maps of the galaxy and its tail. We ensured each sky position was visited by two pixels — the minimum required to produce a good spectral map — to mitigate bad pixel problems. This was achieved by stepping the SL and LL slits in the perpendicular direction by $1.85''$ and $5.1''$, respectively, such that the spectral map was centered about the galaxy. Moreover, during the time of our observations the LL slits were aligned to include the galaxy tail. Figure 1 shows the final configuration of IRS slit positions. We used the outrigger off-source pointings from both LL and SL observations to measure the background and subtracted it from all of our spectra. We removed bad/rogue pixels in two steps. We first masked and interpolated rogue pixels with *IRSCLEAN.MASK* using the SSC rogue pixel map for our observation campaign. Second, we visually inspected the spectral cube for any artifacts along the direction of the slit steps. We manually masked the offending pixel that produced the artifact by first identifying it using the backtracking feature in *CUBISM*, rebuilding the spectral cube, and verifying the artifact was removed. Final on-source integration times per pixel were 235 s, 235 s, 2265 s, and 880 s for the SL1, SL2, LL1, and LL2 spectroscopic cubes, respectively.

For the second IRS dataset (April, 2009), we used the same procedure as the first but with recent versions of the reduced BCD data (version S18.7) and *CUBISM* (version 1.6). The SL slits were stepped in a perpendicular direction by $1.85''$ and covered a region centered immediately west of the galaxy (presumably on the leeward side of the ICM wind) as shown by Figure 1. The pointing was chosen to include both the extraplanar starforming regions and the gas tail immediately after it left the galaxy. The final per pixel integration time for both SL1 and SL2 spectral cubes was 940 s.

The spectra from the different spectrographs and orders were stitched together and placed on a common

wavelength scale in the following manner: The 2nd order spectra of SL and LL were scaled to match the signals in the 1st orders of SL and LL in the regions of wavelength overlap, respectively. Then, the SL data were rescaled to match the LL data. In the case where only LL data were present, the data in the region of wavelength overlap were simply averaged instead of rescaled. For the spectral map centered around the galaxy, we found the $8\mu\text{m}$ flux (derived from a weighted average using the IRAC $8\mu\text{m}$ filter transmission as weights) of the final reduced spectra agreed with the IRAC $8\mu\text{m}$ extended-source corrected flux to within 15%. For the first IRS dataset, the sizes of the final spectral maps are $67'' \times 30''$, $183'' \times 41''$, and $20'' \times 28''$ for SL-only, LL-only, and both SL and LL maps, respectively. For the second dataset, the sizes of the final spectral maps were $59'' \times 16.7''$, $39'' \times 18.4''$ (parallelogram shaped) for SL-only, and both SL and LL maps. When the LL data were combined with the SL data, we interpolated the LL data onto the SL data's pixel grid.

3. RESULTS

3.1. $8\mu\text{m}$ Dust Emission

We present the results of our imaging in Figure 2. The $\text{H}\alpha$ image of ESO137-001 was kindly provided by M. Sun and has been discussed in detail by Sun et al. (2007). There are striking differences between the $3.6\mu\text{m}$ and $8\mu\text{m}$ images. The $3.6\mu\text{m}$ data shows what appears to be a normal spiral galaxy with significant contamination from foreground Milky Way stars. The star-subtracted deep R_C -band image of Woudt et al. (2008), reproduced in Figure 1, shows this galaxy more clearly and confirms it to be undisturbed. However, the $8\mu\text{m}$ image shows a completely different view. We see a cometary structure centered about the galaxy within which are several point-sources. Excess $8\mu\text{m}$ flux is often considered to be from dust, consisting of aromatic hydrocarbons, associated with star formation (Calzetti et al. 2007). To understand the nature of the $8\mu\text{m}$ sources, we first remove the $8\mu\text{m}$ stellar flux to determine the emission from the aromatics. We achieve this by first convolving the $3.6\mu\text{m}$ data to degrade the image quality to match the $8\mu\text{m}$ resolution using kernels provided by Gordon et al. (2008). Then we subtract the convolved $3.6\mu\text{m}$ image after registering it to the $8\mu\text{m}$ image and multiplying it with an arbitrary scaling (~ 0.3) to ensure the bright-stars are properly subtracted. The final subtracted image is presented in Figure 3. The kernel is not perfect because the wings of point-sources are over-subtracted; however, we are able to discern $8\mu\text{m}$ excess clearly. We determine the position of the $8\mu\text{m}$ excess sources by first marking their positions manually, and running a source centroiding program to refine their positions. We present the locations of the sources in Table 1 along with their distances from the center of the galaxy ($\alpha = 16:13:27.30$ and $\delta = -60:45:50.5$) obtained from the NASA Extragalactic Database.

A comparison with the $\text{H}\alpha$ emission shows that the structures and point-sources seen at $8\mu\text{m}$ are also present in the $\text{H}\alpha$ image. In fact, when we do a careful comparison of the two images almost every source at $8\mu\text{m}$ within $1'$ (approximately within the tidal radius) of the galaxy has a clear $\text{H}\alpha$ counterpart with one sole exception, a

source located southeast of the galaxy, also located on the side of the galaxy opposing the tail. It is unclear what this source is, and very likely it is not associated with the galaxy. Overall, the source matching strongly suggests that these $8\mu\text{m}$ excess sources are associated with the galaxy and are relatively young HII regions. This confirms Sun et al. (2007)'s hypothesis that these are star-forming regions, which they arrived at from their analyses of the B-band, I-band, and $\text{H}\alpha$ data.

3.2. The Nature of Star Formation in ESO 137-001

The $\text{H}\alpha$ image clearly shows that the galaxy is currently actively forming stars, a process that is confined to the nuclear region and to a lesser extent along the tail. Our infrared data offer us a complementary look at the star formation activity. We address two questions: 1) Is ESO 137-001 peculiar in any way in its star-forming properties? 2) How does star formation progress in the molecular hydrogen tail? For the first question we look to the IR spectrum of the galaxy (see Figure 6). We focus on the nuclear region, where we have full wavelength coverage across $5 - 36\mu\text{m}$, including the majority of the star formation as indicated by $\text{H}\alpha$ imagery. The spectrum of the galaxy unsurprisingly shows strong aromatic features and an infrared continuum, both clear indicators of on-going star formation. We compare the spectrum with templates provided by Smith et al. (2007) and find it is well-matched with a star-forming galaxy template as shown by Figure 6. We calculate the star-formation rate (SFR) in the central parts of the galaxy by first estimating the MIPS $24\mu\text{m}$ (Rieke et al. 2004) flux from our IRS spectrum multiplied by the MIPS relative response curve.

We use two different approaches to determine the SFR. The prescription from Calzetti et al. (2007) indicates a nuclear SFR of $0.4 M_\odot \text{ yr}^{-1}$. Rieke et al. (2009)'s SFR-to- $24\mu\text{m}$ luminosity also produces a consistent value of $0.4 M_\odot \text{ yr}^{-1}$. We note, however, our galaxy's $24\mu\text{m}$ luminosity falls a factor of 2 lower than the valid range of calibration of the relation in Rieke et al. (2009). Sun et al. (2007) used an extinction-corrected $\text{H}\alpha$ measurement to estimate a SFR of $2 M_\odot \text{ yr}^{-1}$, which translates to $1.3 M_\odot \text{ yr}^{-1}$ for the Kroupa IMF used by Calzetti et al. (2007) and Rieke et al. (2009). Sun et al. (2007) applied a 1.4 mag extinction correction estimated from the $\text{H}\gamma/\text{H}\beta$ line ratio. Reconciling the $\text{H}\alpha$ with the IR-determined SFR, however, would require that there be virtually no extinction to the $\text{H}\alpha$. This seems unlikely because the typical extinction of $\text{H}\alpha$ in integrated measurements of nearby spirals is $1.1 \pm 0.5 \text{ mag}$ (Kennicutt & Kent 1983).

Three effects may contribute to this discrepancy: 1) The simplest one is that the apertures over which the SFR measurements were carried out are not the same. To address this possible issue we present the $\text{H}\alpha$ image convolved to match the $24\mu\text{m}$ IRS resolution and the $24\mu\text{m}$ image of the galaxy, which is shown in Figure 4. The $\text{H}\alpha$ image was convolved using a kernel generated using the $24\mu\text{m}$ IRS PSF computed by stinytim and a modeled PSF of the $\text{H}\alpha$ image using methods outlined in Gordon et al. (2008). The $\text{H}\alpha$ image qualitatively corresponds to the $24\mu\text{m}$ image near the center of the galaxy, though the $\text{H}\alpha$ tail is more extended than the one visible at $24\mu\text{m}$. We also show the extraction apertures used

in the present study and that used by Sun et al. (2007). It is possible that Sun et al. (2007)’s aperture captures more of the $H\alpha$ tail than we do. When we extend our extraction aperture to include both the galaxy and the $24\ \mu\text{m}$ tail, our flux increases by 30%, with a corresponding increase in the SFR. 2) The underlying young stellar populations with strong Balmer absorption lines may be affecting the extinction estimate because the original Sun et al. (2007) spectral observations include light from ESO137-001. This will lead to an overestimate of the extinction correction; the relative contribution of stellar and nebular emission will determine the magnitude of the overestimation. However, as mentioned earlier, it is unlikely that the $H\alpha$ emission suffers from no extinction so this explanation can only account for part of the discrepancy. 3) The $H\alpha$ emission is not solely coming from star-forming regions. This possibility is reaffirmed by the existence of the $H\alpha$ tail in regions with no associated star formation. It is plausible that a combination of all three effects accounts for the discrepancy.

We also checked to see if there are any peculiarities in the aromatic features of ESO 137-001. We fit the nuclear spectrum of the galaxy using PAHFIT (version 1.2; Smith et al. 2007) with extinction correction, and the best fit is shown in Figure 6. We tabulate the strength of various aromatic features in Table 2. The derived flux ratios $L(6.2\mu\text{m})/L(7.7\mu\text{m}\ \text{Complex})$ of 0.29 and $L(11.3\mu\text{m}\ \text{Complex})/L(17\mu\text{m}\ \text{Complex})$ of 2.5 are consistent with star-forming galaxies with HII-dominated nuclei (Smith et al. 2007).

We address the second question, related to the nature of star formation in the molecular hydrogen tail, by comparing the IRAC $8\mu\text{m}$ data and the IRS $24\mu\text{m}$ map with the molecular hydrogen S(1) line map. We first convolve the $8\mu\text{m}$ continuum-subtracted image with a kernel we created using the $17\mu\text{m}$ IRS PSF generated by stinytim and the $8\mu\text{m}$ PSF using the same technique outlined above to degrade the $H\alpha$ image. In Figure 5, we show that the S(1) emission is much more extended than the $8\mu\text{m}$ emission. This is corroborated by our $24\mu\text{m}$ map shown in Figure 4. This means that star-formation only proceeds in the part of the tail that is immediately downstream of the galaxy. Using the techniques outlined above, a $24\ \mu\text{m}$ SFR measurement within the region of the tail with full SL and LL coverage (parallelogram shaped region in Figure 2) produces a value of $0.03\ M_{\odot}\ \text{yr}^{-1}$. The aromatic features measured in this region (tabulated in Table 2), which unlike the nuclear values are not extinction corrected, inhabit the same HII-dominated parameter space as the nuclear values. We conclude a significant portion of the stripped molecular gas may not have high enough density to support star-formation.

3.3. Molecular Hydrogen Tail

In the lower right panel of Figure 2, we show the IRS image taken at the rest-frame $17.035\mu\text{m}\ H_2\ 0-0\ S(1)$ transition. We generated this image by summing up the flux from $17.2-17.4\mu\text{m}$. We find a remarkable tail emanating from ESO137-001 that extends all the way to the edge of the spectral map. This tail is aligned with both the $H\alpha$ and X-ray tails discussed by Sun et al. (2006, 2007) and is at least 20 kpc in length. The undisturbed morphology of the stars in ESO 137-001 (Woudt et al.

2008) plus the unusual state of the gas in the tail eliminate the possibility that it is a tidal feature. Instead, our observations support previous suggestions that the tail arises from ram-pressure stripping (Sun et al. 2006, 2007). We present spectra of this tail in Figures 7 and 8, which were generated by summing up the spectra within the LL-only (shown by the large rectangle in Figure 2) and SL/LL (shown by the parallelogram in Figure 2) regions, respectively. The spectra show strong detections of molecular hydrogen rotational ($H_2\ \nu = 0-0$) lines in this region: the $9.665\ \mu\text{m}\ S(3)$, $12.279\ \mu\text{m}\ S(2)$, $17.035\mu\text{m}\ H_2\ 0-0\ S(1)$, and $28.22\mu\text{m}\ H_2\ 0-0\ S(0)$ transitions.

Molecular hydrogen has multiple pathways that can excite the gas: 1) in regions of strong UV radiation, especially near star-forming sites, H_2 can absorb this radiation and re-emit it as vibration-rotational lines (see Black & van Dishoeck (1987)). This process is known as UV fluorescence. 2) X-ray irradiated molecular gas can also be excited because X-ray photons are able to penetrate the molecular gas clouds deeply and deposit their energy (Maloney et al. 1996). An X-ray dissociation region (XDR) is also set up at the surface of the molecular cloud, which results in a multi-phase structure for the cloud. The outermost surface consists of ionized hydrogen, below which lies neutral hydrogen, and finally molecular hydrogen. 3) Shock-heated molecular gas from high-velocity collisions can also excite molecular hydrogen. In this case, a relatively fast J-shock can dissociate H_2 at the shock only to have it form later on grain surfaces downstream. The lowest J rotational lines are collisionally excited in this process (see Hollenbach & McKee (1989)). Recently, Guillard et al. (2009) have carried out a sophisticated model of the H_2 emission from Stephan’s Quintet. They are able to produce a multiphase medium that emits strongly in rotational molecular hydrogen lines, and to a lesser extent in X-ray and $H\alpha$ from a large galactic scale shock caused by the collision of an intruding galaxy with a tidal arm. The shock-heated gas eventually cools to form molecular H_2 , which is the main coolant in the gas, and is excited by low velocity, non-dissociative magnetohydrodynamic (MHD) shocks that dissipate most of mechanical energy of the collision. Their model adequately explains the two temperature molecular hydrogen component discovered by Appleton et al. (2006). This scenario qualitatively matches our observations. The relatively weak IR continuum, the lack of any aromatic features at $17\ \mu\text{m}$ across the full extent of the tail, and the faint $H\alpha$ tail suggest this feature is likely stripped molecular gas from the galaxy that is either heated by X-rays or through shocks. We may have directly detected the molecular gas from on-going ram pressure stripping of an infalling cluster spiral. This possibility is discussed further in Section 4.3.

4. DISCUSSION

ESO 137-001 has a relatively normal spiral-like stellar distribution and asymmetric gas distribution as evidenced by the X-ray and $H\alpha$ tails. The mere existence of the molecular hydrogen outside the plane of the galaxy raises several interesting questions: How did this molecular gas find its way out of the galaxy? What does this say about galaxy transformation in the cluster environ-

ment? How long does this phenomenon persist? To answer these questions we look at the possible processes that strip galaxies of their gas in clusters. We discuss why tidal stripping processes are not significant, and why ICM gas-stripping is the most likely scenario that explains the observed phenomenon.

4.1. Galaxy-Galaxy Interactions

Galaxy-galaxy interactions can be strong transformative processes in the cluster environment. These interactions can be classified into two broad categories: low speed and high speed interactions. Low speed interactions frequently lead to significant morphological changes and mergers, whereas high speed encounters lead to tidal stripping of gas and stars from the outer edges of disks and induce nuclear starbursts.

If virialized, the high velocity dispersion of Abell 3627 ($\sigma = 925 \text{ km s}^{-1}$; Woudt et al. 2008) makes it a highly unlikely site for a low velocity interaction between two galaxies. However, the case of Abell 3627 is not simple. X-ray imaging of the cluster reveals a subgroup near its center, which is identified in X-ray residuals after subtracting a radially symmetric component. The cluster's diffuse ICM emission is elongated with a position angle of approximately 130° (Böhringer et al. 1996). The central cD galaxy that lies within the subgroup has a peculiar velocity of 561 km s^{-1} with respect to the cluster mean velocity indicating that the cluster is undergoing a merger at its center (Woudt et al. 2008). However, ESO 137-001 lies outside of the subgroup. There is also no compelling evidence that ESO 137-001 is part of a dynamically cooler subgroup (Woudt et al. 2008) making it unlikely for it to have experienced a low velocity encounter with a nearby galaxy. Furthermore, the closest galaxy located within $10'$ with the smallest difference in radial velocity with ESO 137-001 is ESO 136-024, which has a $\Delta v_r = 120 \text{ km s}^{-1}$. One would expect tidally disrupted material to follow the trajectory of the perturber, but the location of ESO 136-024 is not aligned with the tail. In addition, there is no evidence in the stellar morphology (Woudt et al. 2008, see Figure 1) for distortions in the direction of ESO 136-024.

Galaxy harassment in the form of multiple fast interactions in clusters can strip gas and stars from small spiral galaxies and turn them into dwarf elliptical or dwarf spheroidal galaxies (Moore et al. 1996). Simulations show that for high surface brightness spiral galaxies with stellar disk scale lengths of 3 kpc, a value comparable to that measured by Sun et al. (2007) for ESO 137-001, the effect of high speed encounters with massive galaxies is likely to be minor (Moore et al. 1999). In their simulations of tidal interactions, Moore et al. (1999) showed that the disk lost approximately 1 – 2% of the stars and largely retained its disk shape while its disk scale height increased by a factor of 2 – 4 and its disk scale length decreased somewhat. The current disk morphology of ESO 137-001 suggests that if it had an interaction with a massive galaxy, it is likely to have had a minor impact on its stellar distribution. There is no physical reason why the gas would be preferentially stripped over stars in a tidal interaction. Moreover, other simulations show that in tidal interactions, gas typically tracks stars in tidal tails whereas ram-pressure can pro-

duce a significant difference between the stellar and gas distribution (Vollmer 2003; Mayer et al. 2006). In fact, simulations show that tidal interactions often lead to gas inflow and bar formation, and ram-pressure is necessary to strip the gas (Mayer et al. 2006). Additionally, there is a lack of both leading and trailing tails, which are usually present in a tidal interaction (Gavazzi et al. 2001). However, simulations show that it may be possible for ram pressure to erase tidal features produced by a single close encounter and produce long gaseous tails trailing the galaxy (Kapferer et al. 2008). Therefore, the clear difference between the distribution of stars within ESO 137-001 and the gas that trails behind it suggests that tidal interaction between galaxies is not the main contributing factor for the existence of the tail.

4.2. Galaxy-Cluster Tidal Interactions

Inside the cluster core, the deep cluster gravitational potential can also foster galaxy transformation (Henriksen & Byrd 1996). When the cluster tidal force exceeds the galaxy's own restoring force, gas and stars can be tidally stripped from the galaxy and trigger a nuclear starburst (Henriksen & Byrd 1996; Cortese et al. 2007). We calculate the effect of the cluster potential for our galaxy by using the formalism outlined by Henriksen & Byrd (1996). The cluster tidal effect can be expressed as a radial and a transverse acceleration, a_r and a_t , respectively, which are given below:

$$a_t(r) = GM_{cl}(r) \frac{R}{[R^2 + (r + R)^2]^{3/2}} \quad (1)$$

and

$$a_r(r) = GM_{cl}(r) \left[\frac{1}{r^2} - \frac{1}{(r + R)^2} \right] \quad (2)$$

where M_{cl} is the mass of the cluster, r is the distance of the galaxy from the cluster center, and R is the radius of the galaxy. We can calculate the significance of the cluster tidal force by comparing it to the centripetal acceleration of the galaxy, a_{gal} , at the outermost parts of its disk:

$$a_{gal} = \frac{GM_{gal}}{R^2} \quad (3)$$

where M_{gal} is the dynamical mass of the galaxy, and R is the physical extent of the galaxy. On one hand, if the radial tidal acceleration exceeds the centripetal acceleration of the galaxy, we would expect the gas and stars to be stripped by the cluster's gravitation force. On the other hand, if the transverse tidal acceleration exceeds the centripetal acceleration, the gas clouds within the galaxy will be compressed leading to a burst of star formation.

To determine the strength of the cluster tidal acceleration, we first estimate the cluster dynamical mass profile. We tested two approaches to determine the mass: one that uses the X-ray derived dynamical mass profile (Böhringer et al. 1996), and the other that extrapolates to smaller radii using an NFW profile (Navarro et al. 1996) and the dynamical mass estimate determined by Woudt et al. (2008) at large radii. To find the best-fit NFW profile, we use the dynamical mass values for the cluster at 3 different radii (0.67, 1.35, and $2.02 h_{73}^{-1} \text{ Mpc}$)

from Woudt et al. (2008). We use only the virial theorem (M_{VT}) and robust virial M_{RVT} dynamical mass estimates at these radii for our fit. Woudt et al. (2008) suggest that their third method for mass estimation, projected mass estimator, is affected most by substructure, which is present in Abell 3627, and produces a mass estimate that is 50% larger than M_{VT} . M_{VT} and M_{RVT} are least affected by substructure and agree to within 5%, which is why we fit to the average of these two values. Nevertheless, these masses are also likely to be overestimates due to the on-going merger in the cluster. The NFW parameters we obtained were $r_s = 346$ kpc and $c = 6.2$. We do not quote errors on these parameters because error estimates were not given for the mass estimates.

We now compute the relative strengths of the cluster's radial acceleration and the galaxy's centripetal acceleration. The stellar disk is detected out to $40''$ in radius by Sun et al. (2007); this corresponds to a physical distance of 12.6 kpc, which we pick to be the radius of the stellar disk. We estimate the galaxy's dynamical mass by using the K-band velocity-luminosity relation given in Courteau et al. (2007). We obtained a K-band apparent magnitude of 11.6 from a catalogue of galaxies in Abell 3627 (Skelton et al. 2009). We used a distance modulus of 34.1 to obtain a K-band absolute magnitude of -22.5 for the galaxy. For its K-band luminosity, ESO137-001 should have a rotational velocity of 110 km s^{-1} , which coupled with its stellar disk size, corresponds to a dynamical mass of $3.5 \times 10^{10} M_\odot$. In Figure 10, we show the ratio of the cluster's radial and galaxy's centripetal acceleration for the NFW and X-ray gas mass profile. Even at a cluster-centric distance of 280 kpc, the minimum likely separation of the galaxy from the cluster center, we find that the cluster tidal field does not exceed the galaxy's centripetal acceleration. We also calculate the tidal radius of the galaxy at this cluster-centric distance where $a_r/a_{gal} = 1$ using the NFW profile and obtain 15 kpc. This is consistent with the value derived by Sun et al. (2007). Therefore, cluster tidal forces are insufficient to cause any appreciable transformation of the stellar component of the galaxy.

4.3. Gas Stripping

We have shown that the tail emanating from ESO 137-001 cannot result from galaxy interactions or from cluster tidal effects. We now explore the possibility that it arises from ram pressure stripping.

4.3.1. The Effect of Ram Pressure

The fact that the stellar disk appears relatively unperturbed signals that the tail must be generated by a mechanism that only affects gas. ICM ram-pressure stripping (Gunn & Gott 1972) is the most likely candidate. To evaluate this possibility, the cluster-centric radius within which ram-pressure exceeds the galaxy's restoring force can be estimated using the Fujita & Nagashima (1999) reformulation of the Gunn & Gott (1972) criterion:

$$\begin{aligned} \rho_{ICM} v_{gal}^2 &> 2\pi G \Sigma_{star} \Sigma_{HI} \\ &> 2.11 \times 10^{-11} \text{ dyne cm}^{-2} \left(\frac{v_{rot}}{200 \text{ km s}^{-1}} \right)^2 \\ &\quad \times \left(\frac{R}{10 \text{ kpc}} \right)^{-1} \left(\frac{\Sigma_{HI}}{8 \times 10^{20} m_H \text{ cm}^{-2}} \right) \end{aligned} \quad (4)$$

$$(5)$$

where ρ_{ICM} is the density of the ICM, v_{gal} is the velocity of the galaxy with respect to the ICM, v_{rot} is the rotational velocity of the galaxy, R is the radius of the disk, Σ_{HI} is the surface density of the HI disk, and m_H is the mass of the hydrogen atom. Böhringer et al. (1996)'s β -model fit (Cavaliere & Fusco-Femiano 1978) to their ROSAT X-ray data provides an estimate of ρ_{ICM} . We use the β -model parameter values of $\rho_0 = 4.82 \times 10^{-27} \text{ g cm}^{-3}$, $r_X = 184.5$ kpc, and $\beta = 0.555$ to compute the ICM density as a function of cluster-centric radius. We also use the rotational velocity and radial extent of the galaxy given in Section 4.2. The HI surface density and the 3D velocity of this galaxy are unknown. Broeils & Rhee (1997) and Karachentsev et al. (1999) have shown that the HI surface density of spiral galaxies is fairly constant irrespective of the Hubble type or rotational velocity. Karachentsev et al. (1999) specifically looked at a nearby volume-limited sample of galaxies and found the HI surface density had a weak dependence on a galaxy's rotational velocity at less than the 1σ level. The studies give slightly different mean surface densities. Broeils & Rhee (1997) compute an average surface density of $3.8 \pm 1.1 M_\odot \text{ pc}^{-2}$ for their sample of spirals and irregulars. From the HI surface density - rotational velocity relation shown in Karachentsev et al. (1999), we estimate a surface density of $6.3 M_\odot \text{ pc}^{-2}$. For our calculations we were conservative and chose the higher surface density, as that increases the minimum pressure required for ram-pressure stripping. For the galaxy velocity, we picked the values that bound a galaxy's speed in a virialized cluster: σ (925 km s^{-1}) and $\sqrt{3}\sigma$ (1602 km s^{-1}) where σ is the velocity dispersion of the cluster. As an additional check we compute the Mach number of the galaxy using the X-ray data from Sun et al. (2006). Assuming the galaxy is experiencing a shock as it travels through the ICM, we can predict the Mach number if we know the density and temperature of the head of the X-ray tail and the ICM. Sun et al. (2006) quote an average electron density and temperature for the head of the tail to be $1.8 - 3.5 \times 10^{-2} f^{-1/2} \text{ cm}^{-3}$ and 0.64 keV , respectively, where f is the filling factor. The ICM on the other hand has a temperature of 6.3 keV and an electron density of $1.4 \times 10^{-3} \text{ cm}^{-3}$ at the location of the galaxy (Sun et al. 2006). If we assume a filling factor of 1, we obtain a Mach number that ranges from 1.1 – 1.6. Using the ICM sound speed of approximately 800 km s^{-1} that we calculate in Section 4.3.3, we obtain a galaxy velocity through the ICM of $880 - 1280 \text{ km s}^{-1}$. This matches closely with our assumed value, suggesting that the galaxy cannot be moving significantly faster than our predictions.

For a galaxy traveling at a velocity of 925 km s^{-1} , ram-pressure stripping will become significant at cluster-centric radii less than 0.72 Mpc. However, if the galaxy is traveling at 1602 km s^{-1} the radius increases to 1.4 Mpc. Because ESO 137-001 has a very low line-of-sight velocity with respect to the cluster ($\sim 77 \text{ km s}^{-1}$), its true distance from the cluster center is not likely to be much larger than its projected distance. Boselli & Gavazzi (2006) state that infalling galaxies typically follow highly eccentric orbits. We can estimate the cluster-centric distance of the galaxy assuming a roughly linear orbit with

the following equation:

$$r = \frac{R}{\cos(\sin^{-1}(v_{los}/v_{gal}))} \quad (6)$$

where r is the cluster-centric distance, R is the projected distance from the cluster center, v_{los} the line-of-sight velocity of the galaxy, and v_{gal} the 3D velocity of the galaxy. The two galaxy velocity limits mentioned previously put the galaxy at a clustercentric distance of approximately 280 kpc. The galaxy is well within the minimum radius limits where ram-pressure should be a significant transformative process.

4.3.2. Tail Properties and Mass

We calculate the physical properties of the stripped molecular hydrogen by assuming an optically-thin, single (or double) temperature gas model. We first compute the column density of each line, $N_{S(i)}$, using the following equation:

$$N_{S(i)} = \text{flux}_{S(i)} / (A_{S(i)} \times h\nu_{S(i)}) \times 4\pi / \Omega \quad (7)$$

where flux is determined using *PAHFIT* (version 1.2; Smith et al. 2007), which fits for both the continuum and lines, $A_{S(i)}$ is the Einstein A-coefficient for a given transition obtained from Turner et al. (1977), $\nu_{S(i)}$ is the frequency of the transition (values are tabulated in Black & van Dishoeck (1987)), and Ω is the solid angle of the aperture used. We do not include any extinction correction in the fit of the lines because it is likely to be low in the tail region outside of the galaxy. We present the excitation diagram ($\ln(N_{S(i)}/g_u)$ versus T_u) from the observed ground-state rotational transitions in the LL-only region and SL/LL region in Figure 9. g_u and T_u represent the degeneracy and transition energy expressed in terms of the temperature of the upper level of the transition. The degeneracy g for molecular hydrogen can be expressed as $(2J + 1)$ for even/para states (i.e. $J = \text{even}$) and $3(2J + 1)$ for odd/ortho states (i.e. $J = \text{odd}$). We have firm detections of the S(0) and S(1) lines in the LL-only region and S(0), S(1), S(2), S(3), and S(7) lines in the SL/LL region. The S(7) line was extracted from a smaller region within the SL/LL region approximately 1/6 the size of that region to maximize signal-to-noise. See Figure 2 for the location of the S(7) extraction region. From the excitation diagram, we can infer that there are multiple temperature components in the molecular hydrogen tail within the SL/LL region.

Due to the lack of electrical dipole moment in the hydrogen molecules, the only allowed radiative transitions between rotational states require $\Delta J = \pm 2$. Therefore, ortho and para states are radiatively decoupled. The ortho/para ratio (OPR) of molecular hydrogen in local thermodynamic equilibrium (LTE) varies from ~ 1.5 at 100 K to ~ 3 at > 200 K (Burton et al. 1992). The lack of radiative coupling requires collisions between molecules (and/or a catalyst) to reach LTE. The warm component of the molecular hydrogen has temperatures that typically fall within this range of temperatures. Consequently, the OPR may not conform with the LTE value if the hydrogen molecules formed at temperatures higher than 200 K and have now cooled to temperatures lower than 200 K without sufficient density to reach LTE. The OPR is then frozen to the value when the gas was last

in LTE. We carry out a test outlined by Roussel et al. (2007) to check if the observed population is not in LTE. They characterize any deviation from LTE with the $OPR_{\text{high } T}$ parameter, which is the OPR at high gas temperatures. At LTE, $OPR_{\text{high } T}$ is by definition 3.

Roussel et al. (2007) state that if the following condition is satisfied the gas is consistent with a population in LTE: $T(S(0) - S(1)) \leq T(S(0) - S(2)) \leq T(S(1) - S(2)) \leq T(S(1) - S(3)) \leq T(S(2) - S(3))$ where $T(S(i) - S(j))$ is the temperature derived from $S(i)$ and $S(j)$ line ratios. The line ratios of lower excitation energy lines probe components at lower temperatures in a gas with a distribution of temperatures. Temperatures derived from $T(S(0) - S(2))$ and $T(S(1) - S(3))$ are independent of $OPR_{\text{high } T}$, whereas the rest depend on it. The temperatures derived from our lines satisfy the above equality and are consistent with being in LTE. This does not mean the population is definitively in LTE, as it is possible to have slightly lower values of the $OPR_{\text{high } T}$ ratio and still satisfy the condition. However, we assume LTE in our fits of the molecular hydrogen population.

To quantify the physical properties of the gas, we first determined the temperature and total column density (N_{tot}) of the LL-only region by fitting the S(0) and S(1) lines using Equations 8 and 9:

$$\ln(N(T_u)/g_u) = \ln(N_0) - \frac{T_u}{T} \quad (8)$$

where $N(T_u)$ is the column density of a transition, g_u is the degeneracy of the transition, N_0 is the column density of the $J = 0$ state, T_u is the energy (in Kelvin) of the upper energy level of the transition, and T is the temperature of the gas.

$$N_{\text{tot}}(T) = \sum_{j=0}^{j=25} g_j N_0 \exp\left(-\frac{T_j}{T}\right) \quad (9)$$

where N_{tot} is the total column density of the gas, j is the rotational state, T_j is the energy of that state. $T_0 = 0$ K, and $T_1 = 170.6$ K for molecular hydrogen. Equation 9 was summed up to the H_2 0-0 $J = 25$ state, which corresponds to an excitation energy of 37728 K, well above the observed temperatures. For the LL-only tail region we obtained a temperature of 167 ± 4 K and a total column density of $1.60^{+0.23}_{-0.20} \times 10^{19} \text{ cm}^{-2}$ where the errors in the column density were determined through Monte Carlo runs. This corresponds to a total mass within the tail of $2.45^{+0.35}_{-0.31} \times 10^7 \text{ M}_\odot$. In Figure 9, the blue line is the best fit temperature model.

Next, we characterized the molecular hydrogen population in the SL/LL region. As shown by Figure 9, we required a model that could account for multiple components with different temperatures. We chose the simplest model consisting of two-temperature components as given in Equation 10.

$$\ln(N(T_u)/g_u) = \ln\left[\exp\left(-\frac{T_u}{T_1}\right) + f_{2,1} \exp\left(-\frac{T_u}{T_2}\right)\right] + \ln(N_{0,1}) \quad (10)$$

where $N_{0,1}$ is the column density of the $J = 0$ state of the first component, T_1 and T_2 are the temperatures

of the first and second components, respectively, and $f_{2,1} = N_{0,2}/N_{0,1}$ where $N_{0,2}$ is the column density of the $J = 0$ state of the second component. We carried out two least-squares fits to the column densities derived for all lines with firm detections: S(0), S(1), S(2), S(3), and S(7). For the first fit, we used the formal errors derived from the fit of the S(7) line. The best fit model (shown in red in Figure 9) provides temperature estimates of 146 ± 2 K and 682 ± 20 K for the two components. This model had a χ^2_{DOF} of 6.7. The total column density for each component was calculated using Equation 9, producing a value of $2.11^{+0.17}_{-0.15} \times 10^{19} \text{ cm}^{-2}$ for the warm and $1.29^{+0.19}_{-0.16} \times 10^{17} \text{ cm}^{-2}$ for the hot components. These values correspond to masses of $2.10^{+0.17}_{-0.15} \times 10^7 M_\odot$ and $1.29^{+0.19}_{-0.16} \times 10^5 M_\odot$ for the warm and hot components, respectively. For the second fit, we increased the error in the S(7) line strength by a factor of 5 to account for a possible systematic error arising from the smaller extraction area for the line. The new fit yielded slightly different temperature values: 141 ± 5 K and 585 ± 55 K for the warm and hot components, respectively. The model χ^2_{DOF} improved slightly to 4.3. The green curve in Figure 9 represents the best fit. The column density of the warm component changed by less than 10% to $2.29^{+0.34}_{-0.28} \times 10^{19} \text{ cm}^{-2}$, whereas the hot component changed by almost a factor of two to $1.99^{+0.70}_{-0.53} \times 10^{17} \text{ cm}^{-2}$. The final masses of the two components were $2.28^{+0.34}_{-0.28} \times 10^7 M_\odot$ (warm) and $1.98^{+0.70}_{-0.53} \times 10^5 M_\odot$ (hot). The results of all fits are tabulated in Table 4. These results show the warm component is dominant, and its mass is largely insensitive to the choice of hot component parameters. For estimating the galaxy mass loss rate, we use the mass contained within the LL-only aperture because it encompasses the full tail.

We compare our results with the other mass estimates of the tail derived from observations in the H α -band (Sun et al. 2006), and the X-ray (Sun et al. 2007). To make these comparisons, we compute the average gas surface density to mitigate issues arising from mismatched apertures. The gas surface density derived from our molecular hydrogen study ranges from $0.3\text{--}0.4 M_\odot \text{ pc}^{-2}$. Both the H α and X-ray estimates rely on additional assumptions that we do not require. Both assume a cylindrical distribution for the gas to estimate an average electron density, which is then used to arrive at the mass of the radiating gas. Moreover, both estimates depend strongly on the filling factor, f , which is unknown. Taking these effects into consideration, we compute a surface density of hydrogen by dividing the mass estimate by the angular extent of the tail and obtain $\sim 2.5 f^{1/2} M_\odot \text{ pc}^{-2}$ for both the H α and X-ray tails. For the X-ray mass value, we use the tail mass from Sun et al. (2006). This is approximately an order of magnitude higher than our estimate if we assume $f = 1$, but agrees well with ours for the plausible value $f = 0.01$. Our measurement of molecular hydrogen mass is robust because it is more independent of the tail geometry and does not require a free-parameter f . There are additional systematic issues in our mass estimate: 1) the IRS slit coverage does not cover the full axial extent of the tail, which causes us to miss some of the H $_2$ emission at the edges; and 2) it

is unclear what fraction of the molecular gas the warm H $_2$ emission represents. Roussel et al. (2007) in their survey of warm molecular hydrogen in SINGS galaxies find that for galaxies with known CO detections warm molecular hydrogen ($T > 100$ K), on average, represents only 10% of the cold molecular hydrogen. It is unclear if we can apply the fraction found in SINGS galaxies to explain the molecular hydrogen that is being stripped when the underlying formation and heating mechanism may be different. One needs to carry out a full census of the stripped gas through CO and HI observations. The exact physical mechanism that excites the stripped gas to produce emission at these different wavelengths is not entirely clear, making it difficult to predict the different states of the stripped gas. Sun et al. (2007) suggest the H α emission can be produced by heating of the stripped gas by the ICM through thermal conduction.

4.3.3. Mass Loss Rate

We adopt the galaxy velocity limits of $925 \text{ km s}^{-1} < v_{gal} < 1602 \text{ km s}^{-1}$ and a ratio $\gamma = M_{total}/M_{H_2}$ for the stripped gas ($1 \leq \gamma \leq 10$). Then, the warm H $_2$ mass loss rate averaged over the entire tail region is $(1.2\text{--}2)\gamma M_\odot \text{ yr}^{-1}$. With just the molecular hydrogen mass loss rate, we can place an upper limit of $(0.5\text{--}1)/\gamma$ Gyr for the amount of time it would take for the galaxy to lose all of its gas if the mass-loss rate is constant. If we assume a highly eccentric orbit, the galaxy will lose all of its gas in a single pass through the cluster core.

We also consider the case where the galaxy is undergoing viscous stripping (Nulsen 1982). This can be a significant stripping process with the same scaling properties as ram-pressure stripping if the gas flow is turbulent. For turbulent flow, the kinematics of the galaxy through a cluster should produce a Reynolds number > 30 . The Reynolds number, Re , is given in terms of the mean-free-path and sound speed in the ICM, λ_{ICM} and c_{ICM} :

$$Re = 2.8 \left(\frac{r_{gal}}{\lambda_{ICM}} \right) \left(\frac{v_{gal}}{c_{ICM}} \right) \quad (11)$$

$$c_{ICM} = \sqrt{\frac{kT}{m_H}} \quad (12)$$

$$\lambda_{ICM} = 11 \left(\frac{T_{ICM}}{10^8 \text{ K}} \right)^2 \left(\frac{10^{-3} \text{ cm}^{-3}}{\rho_{ICM}/m_H} \right) \quad (13)$$

where T is the temperature of the ICM. We assume an ICM temperature of 6.3 keV (Sun et al. 2006). We calculate Re for the galaxy located at 280 kpc from the cluster center for the two velocity limits. We obtain $30 < Re < 52$ for $925 < v_{gal} < 1602 \text{ km s}^{-1}$. We therefore expect that the gas flow across the wake of the galaxy is turbulent. It is plausible that eddies in this part of the tail promote the star formation occurring there. We can also estimate the mass loss rate following the prescription in Nulsen (1982), which is $\dot{M} = \pi r^2 \rho v_{gal}$ where r is the radius of the gas disk and ρ is the density of the ICM. We set the radius of the gaseous disk to be the half-width of the 17.035 μm emission at the galaxy center, which is 3 kpc. We obtain a mass loss rate that ranges from $0.7 < \dot{M} < 1.2 M_\odot \text{ yr}^{-1}$, consistent with the value that we obtained from our warm molecular hydrogen observations.

4.4. Implications

The discovery of a warm molecular hydrogen tail outside a galaxy and beyond the galaxy's tidal radius provides clear evidence that large amounts of gas are being stripped away as the galaxy plunges into the intracluster medium. To place this single discovery in a general context of galaxy transformation the following questions need to be addressed: How rare is this phenomenon? Should it be detectable in all gas-rich infalling cluster galaxies as they interact with intracluster medium? Our estimates show that the galaxy can lose all of its gas in approximately $(0.5 - 1)/\gamma$ Gyr if it follows a plunging orbit within the cluster that is typical for galaxies entering the cluster for the first time. This also means that the galaxy will lose all of its gas in just one pass through the cluster core. Then, the timescale for the existence of the tail is at most $(0.5 - 1)/\gamma$ Gyr, and it is likely shorter because the stripping rate will increase with decreasing cluster-centric distance. CO and HI observations need to be carried out to complete the inventory of gas in the tail and constrain γ . HI radio observations have so far only placed an upper limit on the gas mass of $10^9 M_\odot$ (Sun et al. 2007).

It is likely that all newly infalling galaxies will have a period when their stripped gas is lit up by the ISM/ICM interaction. A literature survey of galaxies with detected tails in H α (Gavazzi et al. 2001; Sun et al. 2007; Yagi et al. 2007) and/or X-ray (Wang et al. 2004; Sun & Vikhlinin 2005; Sun et al. 2006) reveals that these tails are a fairly rare phenomenon. Sun et al. (2006) in their X-ray survey of 25 nearby hot clusters only discovered 2 galaxies with X-ray tails². It seems likely that the gas stripping must be a relatively quick (\sim hundreds of Myr) process.

Another equally interesting question is how molecular hydrogen can exist outside the galaxy within the hot intracluster medium. A simple calculation of the effect of ram-pressure at the location of ESO 137-001 on a spherical molecular cloud 10 pc in radius and $10^4 M_\odot$ in mass reveals that it can only be moved by ram-pressure a few pcs in a 1 Gyr. This means that ram-pressure cannot move whole clouds out of the galaxy. It is possible that molecular clouds may be ablated by the ICM wind and stripped gradually. However, the more likely explanation is the high velocity dissociative shocks arising from the interaction between the ICM and the ISM of the galaxy dissociate the molecular hydrogen within the galaxy only to have it form on grain surfaces when the shocked gas cools (Guillard et al. 2009). It is unclear how the molecular gas is able to survive the harsh ICM environment. Our IRS observations have a resolution of ~ 3 kpc, insufficient to resolve any structure within the molecular hydrogen tail. We do, however, see the strongest molecular hydrogen in the part of the tail that is closest to the galaxy, and its emission grows fainter the further away it is from the galaxy. This likely results from both the destruction of the molecular hydrogen by the ICM and

the gradual loss of the kinetic energy from the ICM-ISM interaction. Given the velocity of the galaxy through the cluster, we can place a lower limit on the lifetime of the warm molecular hydrogen to be 10 – 20 Myr. This number is likely to be larger if the molecular hydrogen exists in the H α and X-ray emitting parts of the tail, which extend to 40 kpc (Sun et al. 2007) and 70 kpc (Sun et al. 2007), respectively.

It is interesting to place in a broader context our result that ESO 137-001 is being stripped of its ISM rapidly. For example, Moran et al. (2007) identify transforming galaxies in two clusters at $z \sim 0.5$ and conclude that there is a rapid truncation of star formation when spiral galaxies approach the cluster cores closely (within 1.5 Mpc in one case, ~ 300 kpc in the other). They use X-ray measurements to deduce that the difference in truncation distances is directly related to the density and distribution of the ICM in the two clusters, consistent with the effect arising through ram pressure stripping. Cortese et al. (2007) report a galaxy ~ 240 kpc from the center of Abell 1689 that appears to have been recently stripped of its ISM. They find a much more massive galaxy ~ 340 kpc from the center of Abell 2667 that has a stripped tail of gas reminiscent of that from ESO 137-001. Bai et al. (2009) point out that the apparently nearly universal form for the infrared luminosity function in clusters, and its resemblance to the field luminosity function, are most easily explained if the cluster transformation process is quick. Wolf et al. (2009) find a population of massive, dusty red galaxies with strong star formation in Abell 901/2. They argue that these are galaxies in the process of transformation in the cluster environment. Because the proportion of such galaxies is much smaller for masses less than $\sim 10^{10} M_\odot$, they believe that these lower mass galaxies must undergo very rapid transformation, while the process must be substantially longer for more massive ones. This mass dependence is also consistent with predictions for ram pressure stripping. Our observation of ESO 137-001 confirms these indirect lines of argument by allowing direct estimation of the mass loss from a moderate-mass galaxy close to a massive cluster core. The lower limit to our estimated ISM mass loss rate ($\gamma = 1$) is already in the range of theoretical estimates for ram pressure stripping. Should there be a significant amount of cold gas in the stripped tail ($\gamma > 1$), then even more mass will be stripped.

To investigate the approximate timescale for ram-pressure stripping as a function of galaxy and cluster properties, we use the scaling relation for the timescale (τ) for instantaneous ram-pressure stripping given by Mori & Burkert (2000).

$$\tau = 390 \left(\frac{F}{0.1} \right)^{1/2} \left(\frac{M_{gal}}{10^{10} M_\odot} \right)^{2/7} \left(\frac{n_{ICM}}{10^{-4} \text{ cm}^{-3}} \right)^{-1/2} \times \left(\frac{v_{gal}}{10^3 \text{ km s}^{-1}} \right)^{-1} \text{ Myr} \quad (14)$$

where F is the galaxy gas fraction, M_{gal} is the dynamical mass of the galaxy, n_{ICM} is the number density of the ICM at the location of the galaxy, and v_{gal} is the velocity of the galaxy through the ICM. Though Mori & Burkert (2000) discuss gas loss in dwarf galaxies and the assumed distribution of gas is somewhat different than disk galax-

² However, this may not be indicative of the true distribution because the X-ray gas in the tail is much cooler than the ICM (Sun et al. 2006) and may be impossible to discern from the hot ICM X-ray emission especially in the core regions where ICM X-ray emission is the highest. Moreover, the observed H α tails are low surface-brightness features that require relatively long integration times to detect them (Gavazzi et al. 2001).

ies, we believe that the trends in τ should approximately reflect what is experienced by disk galaxies. We compute the time scale as a function of cluster X-ray temperature and the galaxy's cluster-centric distance. The β model (Cavaliere & Fusco-Femiano 1978) was used to generate the ICM density curve. X-ray gas profiles of different temperature clusters when scaled to r_{500} , the radius at which the gas density is 500 times the critical density, show a surprisingly similar structure at large radii with significant scatter in central gas density (Croston et al. 2008). Consequently, we chose a central gas density, core radius and β of 0.0183 cm^{-3} , $0.1r_{500}$ and $2/3$, respectively. The central gas density value was derived from the average electron density value of 0.01 cm^{-3} (Croston et al. 2008) and an electron-to-gas density conversion factor of 1.83 for a fully ionized plasma (Ettori 2005). σ , the velocity dispersion of the cluster, in terms of cluster X-ray temperature (T_X), and r_{500} were computed using the following empirical relationships given by Wu et al. (1999) and Gonzalez et al. (2007), respectively:

$$\sigma = 10^{2.49} \times \left(\frac{T_X}{1 \text{ keV}} \right)^{0.64} \text{ km s}^{-1}; \quad (15)$$

$$r_{500} = 1.41 \left(\frac{\sigma}{1000 \text{ km s}^{-1}} \right)^{1.07} \text{ Mpc}. \quad (16)$$

We assumed v_{gal} to be equivalent to σ , which is the most likely value for a galaxy within a relaxed cluster, and $F = 0.1$. If the true velocity of the galaxy is known, the appropriate timescale can be computed by multiplying the ratio of the galaxy velocity and the predicted σ . We show the ram-pressure stripping timescale curves as a function of cluster gas temperature and galaxy cluster-centric distance in Figure 11. The curves are truncated at a radius of $r_{200} = r_{500}/0.6$, which is approximately the virial radius of a cluster. The prediction for ESO 137-001 is shown by the black star. For the galaxy's dynamical mass ($\sim 10^{10.5} M_\odot$) and possible range of velocities, and a cluster temperature of $\sim 6 \text{ keV}$ (Sun et al. 2006), the computation predicts a ram-pressure time scale of approximately 100 Myr, which is consistent with our upper limit of $(0.5 - 1)/\gamma \text{ Gyr}$. The prediction is likely a lower limit for the true timescale due to the somewhat different physical scenario used by Mori & Burkert (2000) to derive their timescale. However, this places an upper limit on γ to be ~ 5 . We also include the two cluster galaxies studied by Cortese et al. (2007), which have stellar tails in Figure 11. The blue stars correspond to 131124-012040 ($M_{gal} \sim 10^{10.6} M_\odot$) in Abell 1689 and the red stars correspond to 235144-260358 ($M_{gal} \sim 10^{11.6} M_\odot$) in Abell 2667. The filled and unfilled stars correspond to the lower and upper limits of the galaxies' cluster-centric radii computed using velocities of σ and $\sqrt{3}\sigma$, respectively. We compute a timescale of approximately 70 and 200 Myr for 131124-012040 and 235144-260358, respectively, both of which apply to the closest possible cluster-centric radius. The location of the galaxies in these model curves suggest that ram-pressure may be most effective when the galaxy approaches the core region during its first pass while it is still rich in gas. The stripping process may be so quick that the effect is not observed in the core even though stripping is most effective there.

This also explains the paucity of galaxies with stellar tails or ionized/molecular hydrogen gas tails.

5. CONCLUSIONS

The main results of this study are:

1) Through *Spitzer* IRS spectral mapping observations, we detect a warm molecular hydrogen tail ($T \sim 140 - 160 \text{ K}$) extending at least 20 kpc from the galaxy ESO 137-001 in the cluster Abell 3627. The full extent of the tail is unknown and is limited by our slit coverage. The tail is co-aligned with both the X-ray (Sun et al. 2006) and the $H\alpha$ (Sun et al. 2007) tail. We measure a total mass of $2.45^{+0.35}_{-0.31} \times 10^7 M_\odot$ within the warm H_2 tail.

2) Multiple temperature components are present in the tail, and we fit a two-temperature-component model to the observed population distribution. We find that the hot component ($T \sim 580 - 680 \text{ K}$) represents approximately 1% of the gas mass of the tail in the region that we observed.

3) We identify star-forming regions in our $8\mu\text{m}$ data by looking for $8\mu\text{m}$ excesses, which coincide with most of the $H\alpha$ regions detected by Sun et al. (2007). We also identify a large $8\mu\text{m}$ excess that resembles a cometary structure centered about the galaxy.

4) We discover the molecular hydrogen tail extends farther than the extent of the star forming regions, which are mostly found within the tidal radius of the galaxy. This suggests that star formation occurs in turbulent pockets within the molecular hydrogen tail.

5) The infrared spectrum of ESO 137-001 itself matches expectations for a normal starforming galaxy. We estimate a star forming rate at the nucleus of $0.4 M_\odot \text{ yr}^{-1}$, which is significantly less than the extinction-corrected value of $2 M_\odot \text{ yr}^{-1}$ estimated by Sun et al. (2007). This discrepancy may be resolved through the use of smaller extinction corrections and/or the allowance of some of the $H\alpha$ to come from a mechanism other than star formation.

6) Assuming a velocity range of $925(\sigma) < v_{gal} < 1602(\sqrt{3}\sigma) \text{ km s}^{-1}$ for the galaxy, we obtain a molecular hydrogen mass loss rate of $(1.2 - 2)\gamma M_\odot \text{ yr}^{-1}$, where γ is the ratio of total gaseous mass to the mass in warm gas ($1 \leq \gamma \leq 10$). Ram-pressure stripping is the most likely explanation for the existence of this tail. A simple calculation of the viscous stripping rate of the galaxy produces a mass loss rate of $1 M_\odot \text{ yr}^{-1}$, which is consistent with the observed value.

8) These results support directly the hypothesis that ram-pressure stripping can transform galaxies quickly when they fall into the cores of massive clusters.

We would like to thank Ming Sun for providing us with his $H\alpha$ data and giving several useful suggestions for the paper. We thank Lisa Storrie-Lombardi for expediting obtaining our follow-up SL spectra. This work was supported by contract 1255094 from Caltech/JPL to the University of Arizona. This research has made use of the NASA/IPAC Extragalactic Database (NED) which is operated by the Jet Propulsion Laboratory, California Institute of Technology, under contract with the National Aeronautics and Space Administration.

REFERENCES

- Appleton, P. N., et al. 2006, *ApJ*, 639, L51
 Bai, L., Rieke, G. H., Rieke, M. J., Christlein, D., & Zabludoff, A. I. 2009, *ApJ*, 693, 1840
 Black, J. H., & van Dishoeck, E. F. 1987, *ApJ*, 322, 412
 Böhringer, H., Neumann, D. M., Schindler, S., & Kraan-Korteweg, R. C. 1996, *ApJ*, 467, 168
 Boselli, A., & Gavazzi, G. 2006, *PASP*, 118, 517
 Broeils, A. H., & Rhee, M.-H. 1997, *A&A*, 324, 877
 Burton, M. G., Hollenbach, D. J., & Tielens, A. G. G. 1992, *ApJ*, 399, 563
 Calzetti, D., et al. 2007, *ApJ*, 666, 870
 Cavaliere, A., & Fusco-Femiano, R. 1978, *A&A*, 70, 677
 Chung, A., van Gorkom, J. H., Kenney, J. D. P., & Vollmer, B. 2007, *ApJ*, 659, L115
 Cortese, L., et al. 2007, *MNRAS*, 376, 157
 Courteau, S., Dutton, A. A., van den Bosch, F. C., MacArthur, L. A., Dekel, A., McIntosh, D. H., & Dale, D. A. 2007, *ApJ*, 671, 203
 Croston, J. H., et al. 2008, *A&A*, 487, 431
 Dressler, A. 1980, *ApJ*, 236, 351
 Ettori, S. 2005, *MNRAS*, 362, 110
 Fazio, G. G., et al. 2004, *ApJS*, 154, 10
 Fujita, Y., & Nagashima, M. 1999, *ApJ*, 516, 619
 Gavazzi, G., Boselli, A., Mayer, L., Iglesias-Paramo, J., Vílchez, J. M., & Carrasco, L. 2001, *ApJ*, 563, L23
 Gonzalez, A. H., Zaritsky, D., & Zabludoff, A. I. 2007, *ApJ*, 666, 147
 Gordon, K. D., Engelbracht, C. W., Rieke, G. H., Misselt, K. A., Smith, J.-D. T., & Kennicutt, R. C., Jr. 2008, *ApJ*, 682, 336
 Guillard, P., Boulanger, F., Pineau Des Forêts, G., & Appleton, P. 2009, *astro-ph/0904.4239v2*
 Gunn, J. E., & Gott, J. R. I. 1972, *ApJ*, 176, 1
 Henriksen, M., & Byrd, G. 1996, *ApJ*, 459, 82
 Hollenbach, D., & McKee, C. F. 1989, *ApJ*, 342, 306
 Houck, J. R., et al. 2004, *ApJS*, 154, 18
 Kapferer, W., Kronberger, T., Ferrari, C., Riser, T., & Schindler, S. 2008, *MNRAS*, 389, 1405
 Karachentsev, I. D., Makarov, D. I., & Huchtmeier, W. K. 1999, *A&AS*, 139, 97
 Kawata, D., & Mulchaey, J. S. 2008, *ApJ*, 672, L103
 Kennicutt, R. C., Jr., & Kent, S. M. 1983, *AJ*, 88, 1094
 Koopmann, R. A., & Kenney, J. D. P. 2004, *ApJ*, 613, 866
 Maloney, P. R., Hollenbach, D. J., & Tielens, A. G. G. M. 1996, *ApJ*, 466, 561
 Mayer, L., Mastropietro, C., Wadsley, J., Stadel, J., & Moore, B. 2006, *MNRAS*, 369, 1021
 Moore, B., Katz, N., Lake, G., Dressler, A., & Oemler, A. 1996, *Nature*, 379, 613
 Moore, B., Lake, G., Quinn, T., & Stadel, J. 1999, *MNRAS*, 304, 465
 Moran, S. M., Ellis, R. S., Treu, T., Smith, G. P., Rich, R. M., & Smail, I. 2007, *ApJ*, 671, 1503
 Mori, M., & Burkert, A. 2000, *ApJ*, 538, 559
 Navarro, J. F., Frenk, C. S., & White, S. D. M. 1996, *ApJ*, 462, 563
 Nulsen, P. E. J. 1982, *MNRAS*, 198, 1007
 Ogle, P., Antonucci, R., Appleton, P. N., & Whysong, D. 2007, *ApJ*, 668, 699
 Rieke, G. H., et al. 2004, *ApJS*, 154, 25
 Rieke, G. H., Alonso-Herrero, A., Weiner, B. J., Pérez-González, P. G., Blaylock, M., Donley, J. L., & Marcillac, D. 2009, *ApJ*, 692, 556
 Roussel, H., et al. 2007, *ApJ*, 669, 959
 Skelton, R. E., Woudt, P. A., & Kraan-Korteweg, R. C. 2009, *MNRAS*, 392, 724
 Smith, J. D. T., et al. 2007, *PASP*, 119, 1133
 Smith, J. D. T., et al. 2007, *ApJ*, 656, 770
 Sun, M., & Vikhlinin, A. 2005, *ApJ*, 621, 718
 Sun, M., Jones, C., Forman, W., Nulsen, P. E. J., Donahue, M., & Voit, G. M. 2006, *ApJ*, 637, L81
 Sun, M., Donahue, M., & Voit, G. M. 2007, *ApJ*, 671, 190
 Tonnesen, S., Bryan, G. L., & van Gorkom, J. H. 2007, *ApJ*, 671, 1434
 Turner, J., Kirby-Docken, K., & Dalgarno, A. 1977, *ApJS*, 35, 281
 Vollmer, B. 2003, *A&A*, 398, 525
 Wang, Q. D., Owen, F., & Ledlow, M. 2004, *ApJ*, 611, 821
 Wolf, C., et al. 2009, *MNRAS*, 393, 1302
 Woudt, P. A., Kraan-Korteweg, R. C., Lucey, J., Fairall, A. P., & Moore, S. A. W. 2008, *MNRAS*, 383, 445
 Wu, X.-P., Xue, Y.-J., & Fang, L.-Z. 1999, *ApJ*, 524, 22
 Yagi, M., Komiyama, Y., Yoshida, M., Furusawa, H., Kashikawa, N., Koyama, Y., & Okamura, S. 2007, *ApJ*, 660, 1209

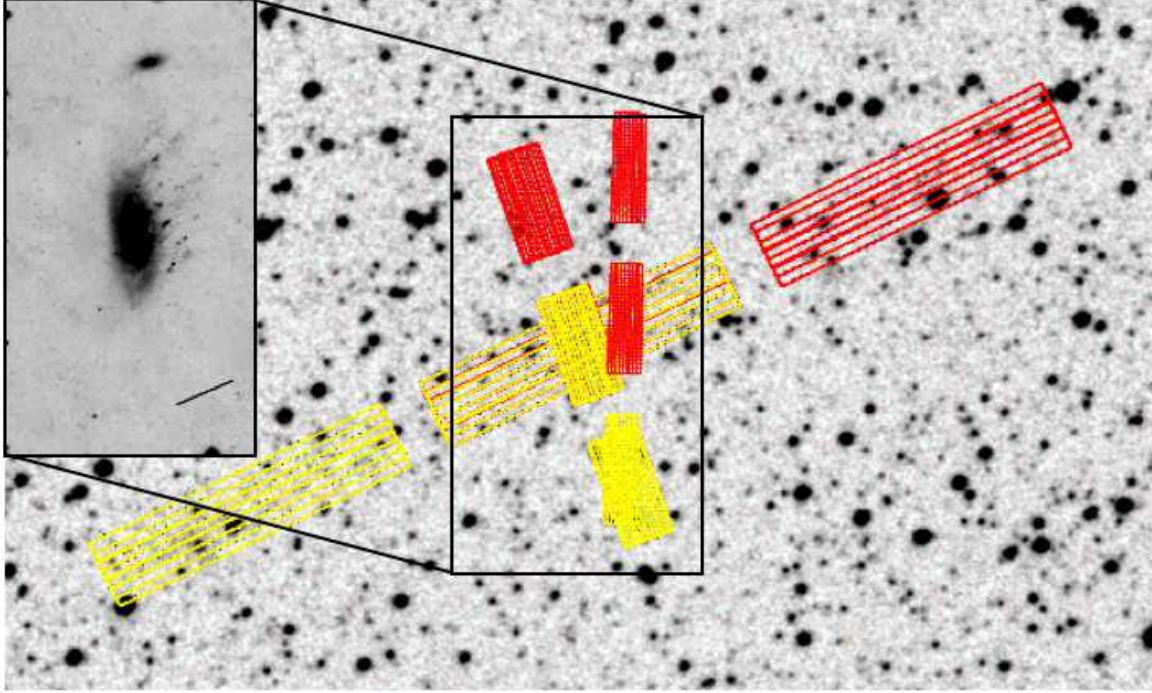


FIG. 1.— 6' by 10' Digital Sky Survey Image centered about ESO 137-001 with our IRS pointings overlaid. North is up and East is left. Background subtraction is carried out by outrigger slit pointings. The inset is the 2.2' by 4' star-subtracted R_C -band image of ESO 137-001 reproduced from Figure 10 of Woudt et al. (2008). This image has been contrast enhanced to reveal low surface brightness features. The diagonal line shown in the inset is the direction of elongation of the E/S0 population discussed in Woudt et al. (2008), which lies very close in position angle to the X-ray and $H\alpha$ tails. We chose the long-low slits to be coaligned with the X-ray tail discovered by Sun et al. (2006).

TABLE 1
DUSTY $8\mu\text{m}$ SOURCE LIST

#	RA	DEC	Distance (")	$H\alpha$ counterpart
1	16:13:27.225	-60:45:50.69	0.6	Y
2	16:13:24.906	-60:45:51.37	17.5	Y
3	16:13:26.399	-60:45:33.95	18.3	Y
4	16:13:24.954	-60:45:43.82	18.6	Y
5	16:13:25.499	-60:45:34.95	20.8	Y
6	16:13:24.160	-60:45:55.05	23.4	Y
7	16:13:24.568	-60:46:05.96	25.0	Y
8	16:13:23.747	-60:45:52.99	26.1	Y
9	16:13:24.130	-60:45:32.66	29.6	-*
10	16:13:23.545	-60:45:23.80	38.7	Y
11	16:13:25.730	-60:45:09.53	43.0	Y
12	16:13:29.781	-60:46:30.29	43.3	N
13	16:13:22.995	-60:45:21.06	43.5	Y
14	16:13:23.029	-60:44:49.35	69.1	Y
15	16:13:32.006	-60:47:00.35	77.4	N
16	16:13:36.141	-60:44:53.39	86.7	-
17	16:13:30.064	-60:47:25.97	97.1	-
18	16:13:42.597	-60:46:28.61	118.2	-
19	16:13:25.845	-60:43:48.14	123.3	-*
20	16:13:46.649	-60:45:55.85	141.8	-
21	16:13:08.670	-60:46:46.56	147.3	-*
22	16:13:37.556	-60:43:39.70	151.3	-
23	16:13:04.917	-60:46:17.42	166.1	-
24	16:13:27.176	-60:48:54.68	183.7	-

* The location of these sources have been blocked in the $H\alpha$ image due to their close proximity to bright stars.

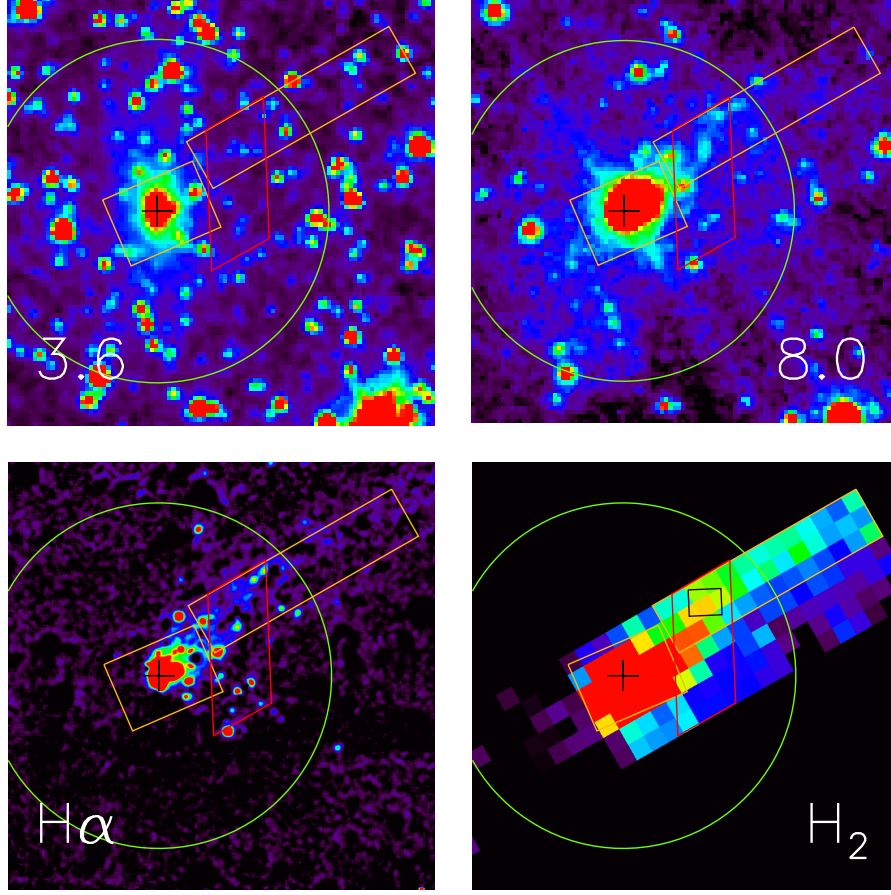


FIG. 2.— $2'$ by $2'$ images of ESO 137-001 at $3.6\mu\text{m}$, $8\mu\text{m}$, $\text{H}\alpha$ (Sun et al. 2007), and rest $17.035\mu\text{m}$ (H_2 0-0 S(1) transition) wavelengths. North is up and East is left. The $\text{H}\alpha$ image is smoothed to $1.2''$ resolution. The colors follow the visible spectrum, where blue represents the faintest emission, and red the brightest. The center of the galaxy is shown with a black cross. The polygons outline the spectral extraction regions. The box that is centered about the galaxy is termed the nuclear region and includes both short-low (SL) and long-low (LL) coverage. The red trapezoid includes full SL and LL coverage of the tail and is identified as the SL/LL tail region, while the large rectangular box that encloses the full extent of the molecular hydrogen tail has only LL coverage and is termed the LL-only tail region. The spectrum within the small black box located in the SL/LL tail region was used to fit the H_2 0-0 S(7) line. The large green circle centered about the galaxy is the tidal radius. The $3.6\mu\text{m}$ image shows a relatively undisturbed spiral galaxy. We observe a cometary structure at $8\mu\text{m}$ that strongly suggests ram pressure stripping. We also see a strong correspondence between the $8\mu\text{m}$ and $\text{H}\alpha$ images, which is expected for star-forming regions. The morphologies at $\text{H}\alpha$ and $8\mu\text{m}$ do not correspond to the $3.6\mu\text{m}$ image, suggesting that the star forming regions are relatively young. A strikingly long molecular hydrogen tail is shown in the $17.035\mu\text{m}$ image. The position angles of the tails seen in $\text{H}\alpha$ and $8\mu\text{m}$ are colligned with the molecular hydrogen tail. This is evidence for warm gas being stripped from a galaxy with knots of star formation within it.

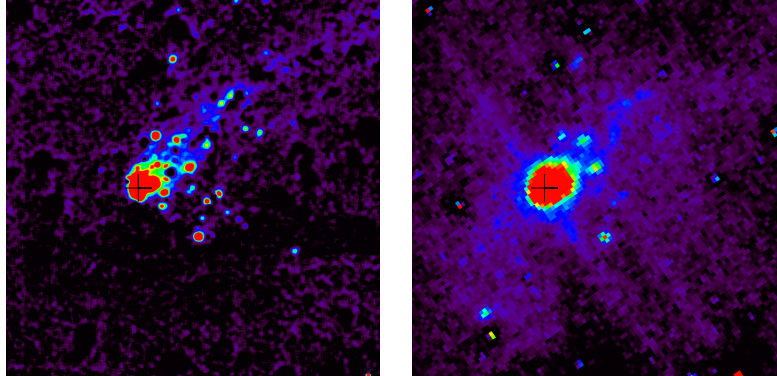


FIG. 3.— $2'$ by $2'$ $\text{H}\alpha$ image (left) of ESO 137-001 smoothed to $1.2''$ resolution and the corresponding stellar continuum subtracted $8\mu\text{m}$ image (right). The colors follow the visible spectrum, where blue represents the faintest emission, and red the brightest. Every source present in the $8\mu\text{m}$ image is present in the $\text{H}\alpha$ image with the exception of the point source southeast from the galaxy. It is unclear what this source is. The similarity between the two wavelengths establishes the $\text{H}\alpha$ and $8\mu\text{m}$ sources are likely star-forming regions. These sources are in a fan-like configuration downstream of the galaxy.

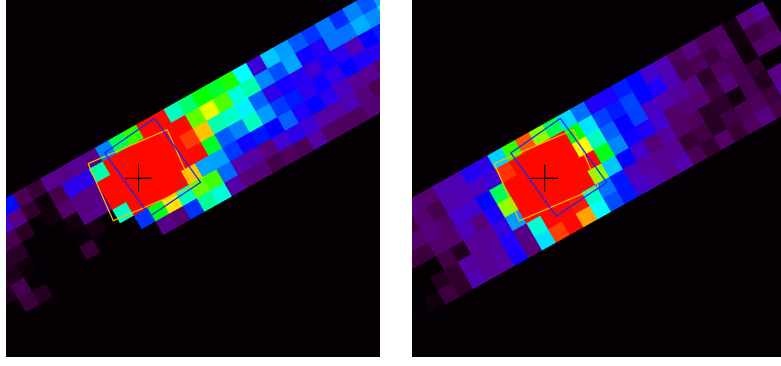


FIG. 4.— $2'$ by $2'$ images of ESO 137-001 at $H\alpha$ degraded to IRS $24\mu m$ resolution (left) and the rest $24\mu m$ image (right). The colors follow the visible spectrum, where blue is represents the faintest emission, and red the brightest. The center of the galaxy is shown with a black cross. The orange box is the spectral extraction region used to measure the SFR. The blue box is the region used by Sun et al. (2007) to compute their $H\alpha$ SFR. The $24\mu m$ emission, a proxy for star-formation, qualitatively follows the $H\alpha$ emission in the nuclear regions but is not as extended. It is also not as extended as the molecular hydrogen emission and more closely follows the $8\mu m$ emission.

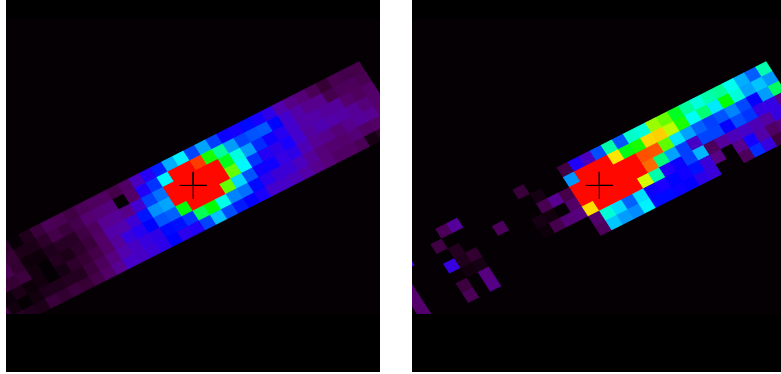


FIG. 5.— $2.5'$ by $2.5'$ images of ESO 137-001 at $8\mu m$ [left] and rest $17.035\mu m$ (H_2 0-0 S(1)) wavelength [right]. The colors follow the visible spectrum, where blue is represents the faintest emission, and red the brightest. The $8\mu m$ data was smoothed to match the $17\mu m$ resolution after subtracting the stellar continuum using $3.6\mu m$ data. The center of the galaxy is shown with a black cross. The long-low spectrograph spatial coverage is shown by the orange box in the convolved $8\mu m$ image. Though there is some correspondence between the $8\mu m$ and molecular hydrogen emission, the molecular hydrogen tail is more extended than the $8\mu m$ emission. This hints that the stripped molecular hydrogen must only have sufficient density to form stars shortly after it has been removed from the galaxy.

TABLE 2
AROMATIC FEATURE FLUXES

Aromatic Feature	Nuclear Flux ($10^{-17} \text{ W m}^{-2}$)	Tail (SL/LL Region) Flux ($10^{-17} \text{ W m}^{-2}$)
$6.2 \mu m$	70.7 ± 2.2	2.65 ± 0.76
$7.7 \mu m$ Complex	239 ± 7	31.0 ± 2.6
$11.3 \mu m$ Complex	56.0 ± 0.7	5.62 ± 0.29
$12.6 \mu m$ Complex	31.7 ± 0.9	1.98 ± 0.35
$17.7 \mu m$ Complex	22.0 ± 0.3	1.39 ± 0.09

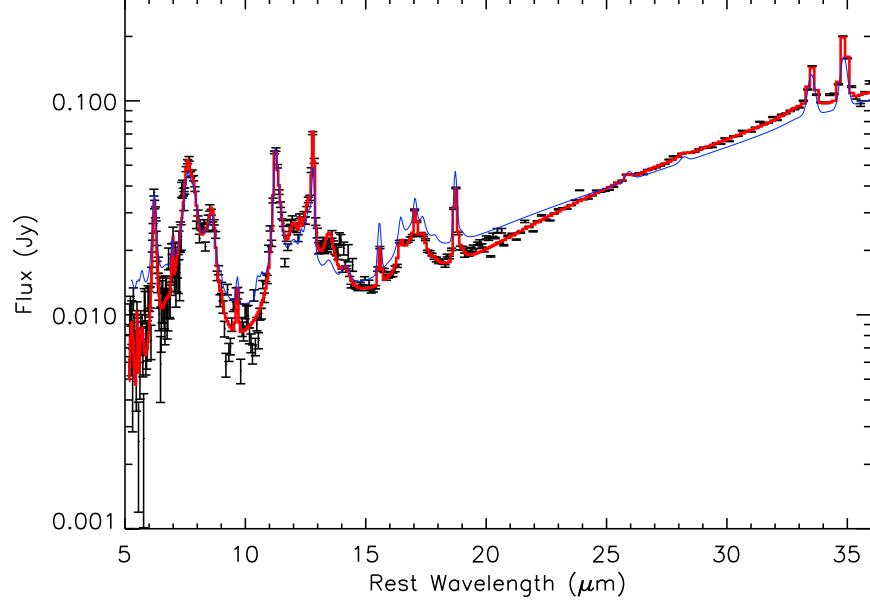


FIG. 6.— ESO 137-001 nuclear region rest-frame spectrum. The red line denotes the best fit to the data. We have full short-low and long-low spectrograph coverage in this region. The blue line is a starforming galaxy template spectrum from Smith et al. (2007). The template spectrum was rescaled to match the $24\ \mu\text{m}$ flux of ESO 137-001. We see a fairly good match between the two spectra, suggesting there is nothing peculiar about the infrared properties of ESO 137-001.

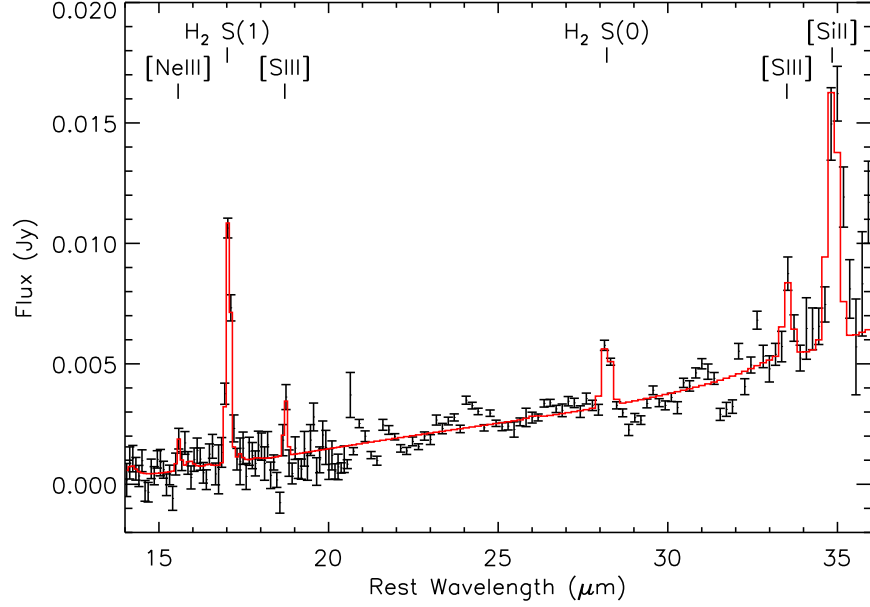


FIG. 7.— ESO 137-001 LL-only tail region rest-frame spectrum. The red line denotes the best fit to the data. The spectrum shows strong H_2 0-0 S(1) and S(0) transitions in addition to atomic fine structure lines.

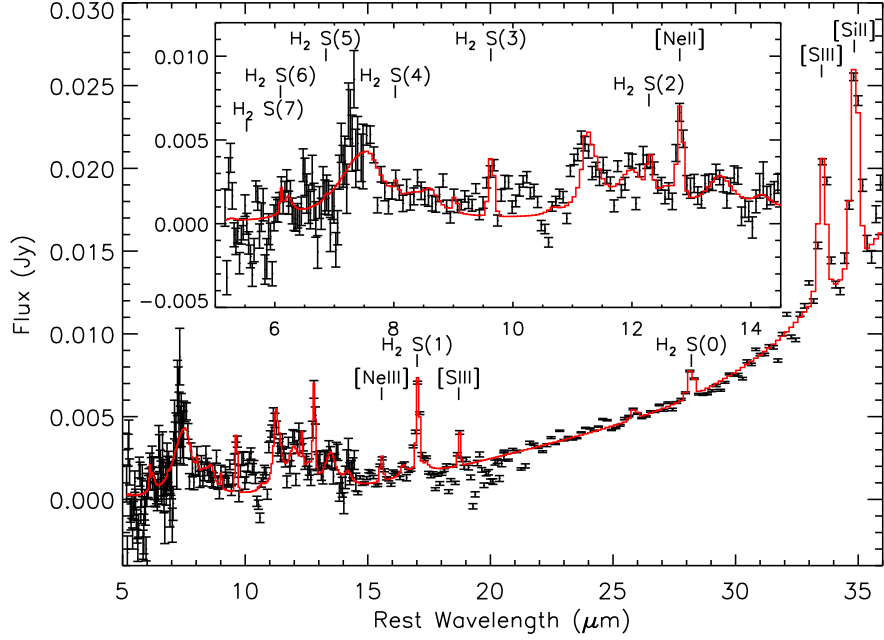


FIG. 8.— ESO 137-001 SL/LL tail region rest-frame spectrum. The SL data are shown with a larger stretch within the inset plot. The red line denotes the best fit to the data. Atomic fine structure and H_2 0-0 S(0) thru S(3) lines are detected at greater than 3σ significance within this region. The presence of aromatic emission indicates star-formation is occurring in this region.

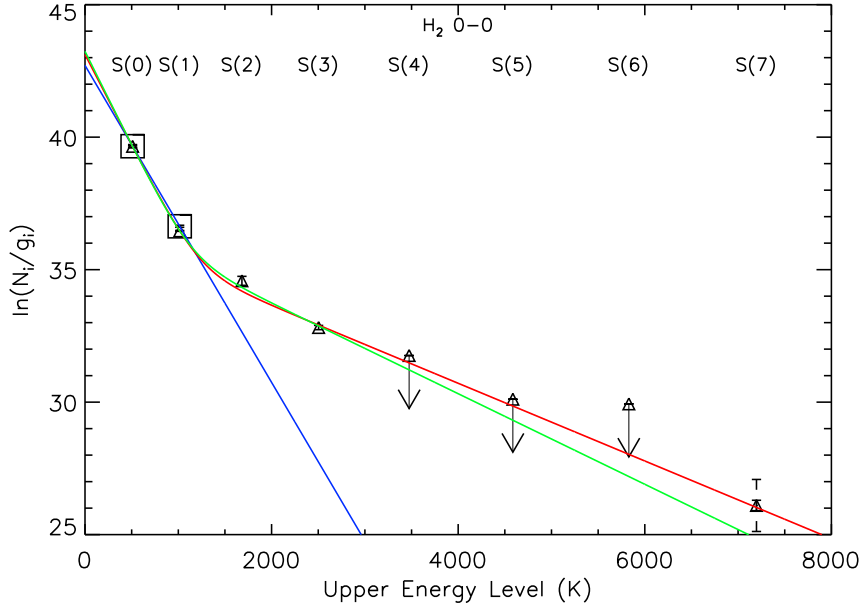


FIG. 9.— Excitation diagram for the molecular hydrogen tail. The square points and triangular points represent the populations in the LL-only and SL/LL tail regions, respectively. The LL-only region was fit by a single temperature, which is represented by the solid blue line. The SL/LL region population was fit by a two-temperature (hot and warm components) model. For the two temperature model fits, the S(0), S(1), S(2), S(3), S(7) lines were included. The S(7) line was extracted within a region approximately 6 times smaller than the SL/LL region to obtain adequate signal to noise. We ran two different two-temperature fits while adjusting the error in the S(7) transition column density. For the first fit (red curve), we used the formal errors derived from the S(7) line flux. For the second fit (green curve), we multiplied the error in the S(7) column density 5 times (shown by the larger error bars in the S(7) data point) to reflect the possibility that the emission may be roughly constrained to only the S(7) extraction region, which will reduce the overall number density of that line by a factor of 5 across the full SL/LL region.

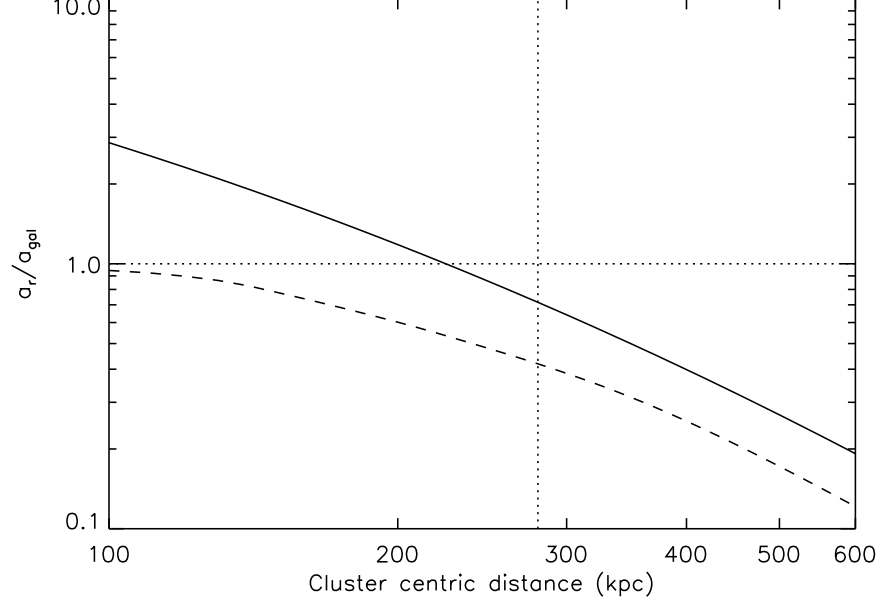


FIG. 10.— Ratio of cluster radial a_r and galaxy centripetal a_{gal} acceleration as a function of cluster-centric distance. The solid and dashed curves represent values determined from a best-fit NFW cluster mass profile and a X-ray-data-derived mass profile, respectively. If the ratio is greater than 1 (the dotted horizontal line), the cluster tidal force will be sufficient to tidally strip the galaxy. However, at the projected distance of 280 kpc (the dotted vertical line), the minimum distance the cluster galaxy can be from the center, the ratio is less than 1 for both cluster mass profiles, indicating that tidal stripping from the cluster gravitational field is not a significant effect.

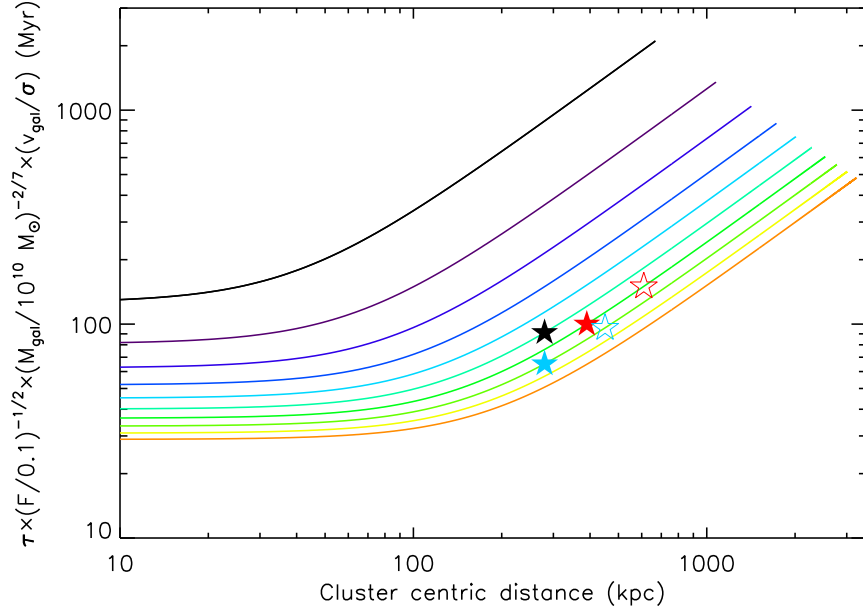


FIG. 11.— Ram-pressure stripping timescale prediction (τ) for different cluster temperatures as a function of cluster-centric distance. The curves are truncated at the virial radii of the simulated clusters. The black line is a 1 keV cluster, and every successive curve increases by 1 keV, where the orange line is 10 keV. The black star is the prediction for ESO 137-001. The blue and red stars are predictions for the cluster galaxies 131124-012040 and 235144-260358, respectively, studied by Cortese et al. (2007), which have stellar trails. The filled and open stars represent the lower and upper radial limits, respectively, for these galaxies. ESO 137-001 is only represented by a single star because its projected distance from the cluster center is also thought to be its true distance from the center due to its low radial velocity with respect to the cluster. The galaxies have relatively quick stripping time scales ranging from 70 – 200 Myr. Moreover, they inhabit a region that is just outside the cluster core where ram-pressure is the strongest. This may indicate that in this mass range experience the most ram-pressure stripping just outside the cluster core where they exhaust most of their gas.

TABLE 3
MEASURED H₂ ROTATIONAL LINE FLUXES FOR ESO 137-001

Spectral Feature	λ (μm)	Tail (SL/LL) Flux ($10^{-17} \text{ W m}^{-2}$)	Tail (LL-only) Flux ($10^{-17} \text{ W m}^{-2}$)
0-0 S(7)	5.511	$0.672 \pm 0.132^{\text{a}}$	—
0-0 S(6)	6.109	$< 0.735^{\text{b}}$	—
0-0 S(5)	6.909	$< 1.06^{\text{b}}$	—
0-0 S(4)	8.026	$< 0.618^{\text{b}}$	—
0-0 S(3)	9.665	1.40 ± 0.11	—
0-0 S(2)	12.279	0.49 ± 0.08	—
0-0 S(1)	17.035	0.93 ± 0.02	1.80 ± 0.07
0-0 S(0)	28.221	0.20 ± 0.01	0.33 ± 0.02

^a The flux of this line was extracted over a smaller region within the SL/LL tail aperture. The area of the extraction region $0.155 \times$ the area of the SL/LL tail aperture.

^b 3σ detection limits for lines.

TABLE 4
MEASURED H₂ GAS MASSES FOR ESO 137-001

Fit	Component	T_{ex} (K)	N_{tot} (cm^{-2})	Σ ($\text{M}_{\odot} \text{ pc}^{-2}$)	H ₂ Mass (M_{\odot})
Tail (LL-only)	Warm	167 ± 4	$1.60^{+0.23}_{-0.20} \times 10^{19}$	$0.26^{+0.04}_{-0.03}$	$2.45^{+0.35}_{-0.31} \times 10^7$
Tail (SL/LL)	Warm	146 ± 2	$2.11^{+0.17}_{-0.15} \times 10^{19}$	$0.34^{+0.03}_{-0.02}$	$2.10^{+0.17}_{-0.15} \times 10^7$
	Hot	682 ± 20	$1.29^{+0.19}_{-0.16} \times 10^{17}$	$2.06^{+0.30}_{-0.26} \times 10^{-3}$	$1.29^{+0.19}_{-0.16} \times 10^5$
Tail (SL/LL)	Warm	141 ± 5	$2.29^{+0.34}_{-0.28} \times 10^{19}$	$0.37^{+0.05}_{-0.04}$	$2.28^{+0.34}_{-0.28} \times 10^7$
High S(7) Error	Hot	585 ± 55	$1.99^{+0.70}_{-0.53} \times 10^{17}$	$3.18^{+1.12}_{-0.85} \times 10^{-3}$	$1.98^{+0.70}_{-0.53} \times 10^5$